Influence of ferroelectric order on the surface electronic structure of BaTiO₃ films studied by photoemission spectroscopy

Stefan Muff,[1,2] Nicolas Pilet,[2] Mauro Fanciulli,[1,2] Andrew P. Weber,[1,2] Christian Wessler,[2]
Zoran Ristić,[2] Zhiming Wang,[2,3] Nicholas C. Plumb,[2] Milan Radović,[2] and J. Hugo Dil[1,2]

[1]*Institut de Physique, École Polytechnique Fédérale de Lausanne, CH-1015 Lausanne, Switzerland*
[2]*Photon Science Division, Paul Scherrer Institut, CH-5232 Villigen, Switzerland*
[3]*Department of Quantum Matter Physics, University of Geneva, CH-1211 Geneva 4, Switzerland*

The electronic structure of *in situ* grown ferroelectric BaTiO₃(001) films is studied by angle-resolved photoemission spectroscopy. A two-dimensional state is found at the film-vacuum interface with an unexpected checkerboardlike Fermi surface. The observed absence of in-plane dispersion of the states is attributed to the influence of the strong electric fields of the ferroelectric bulk of the film. These fields cause Bloch oscillations and Wannier-Stark localization of free charges in real space, resulting in a smearing in reciprocal space. It is shown that this effect extends to thin SrTiO₃ overlayers grown on the BaTiO₃ film.

I. INTRODUCTION

Ferroelectric and magnetoelectric materials are expected to play an important role in future electronics because of their nonvolatile properties and possible switching by electric fields. However, the influence of ferroelectricity on the electronic structure has only received limited attention. One of the reasons is that a large enough free charge carrier concentration will cause the ferroelectric order to break down, although where this limit lies is still an open question [1–3]. Recently, it was shown that the atomic displacement and inversion symmetry breaking associated with ferroelectric order leads to a switchable Rashba-type spin splitting of the bulk bands in semiconducting GeTe [4–6]. This raises the question as to what will happen to electronic states at the Fermi level of a ferroelectric material based on transition metal oxides (TMOs) with low enough free charge density, or for a conductive material in close proximity to such a ferroelectric.

Of particular interest is the influence of the large local electric field induced by the ferroelectric order. If these fields are oriented along a direction where no charge flow is possible, they lead to a variety of Rashba-type effects, such as recently predicted for transition metal dichalcogenide monolayers [7]. On the other hand, the situation is less clear for the situation when the field is oriented along a direction where the charge can flow. In this work, we explore a possible response of the system to this situation based on our experimental observations.

Electric fields are the driving force of electric transport and a variety of electronic properties of semiconductor systems. The ultimate limiting mechanism of conductance in crystals is defect scattering, which prevents ballistic transport. However, in an ideal system, without defect scattering, electrons would perform an oscillating motion for large enough electric fields. These so-called Bloch oscillations form due to the Bragg scattering of the accelerated electrons at the Brillouin zone boundary [8,9]. The oscillations eventually lead to a Wannier-Stark localization (WSL) of the accelerated electrons as well as

the formation of a Wannier-Stark ladder [10,11]. These effects set a fundamental limit to coherent transport in crystals and their existence in a real system will provide further insight into its transport mechanisms.

The Bloch oscillation time for one cycle is given by $\tau_B = h/(eFa)$, where h is the Planck constant, e the electron charge, F the electric field present, and a the lattice parameter in the direction of the electric field. In real crystals, the critical condition for Bloch oscillations to be possible is a τ_B smaller than the relaxation time τ of the system which is determined by the mean-free path λ and the Fermi velocity v_F. In other words, the electron has to complete one (or several) periods of the Bloch oscillation before being scattered at random lattice defects. This condition can not be met by applying an external electric field on single-crystal semiconductors because the required fields are orders of magnitudes higher than the breakdown voltages of these systems. This problem was successfully addressed by the engineering of artificial semiconductor lattices of high quality. In artificial superstructures, the lattice parameter a is increased and thus the required electric field is lowered to an achievable value to observe Bloch oscillations and related effects [12–17]. These issues have made optical lattices with ultracold atoms a method of choice to study this physics [18,19]. Alternatively, Bloch oscillations can also be induced for a short timescale using terahertz radiation [20].

Here, we suggest a different way in which such Bloch oscillations can be induced, namely, due to the large local electric fields experienced by a conductor in close proximity to a ferroelectric. Based on the measured angle-resolved photoelectron spectroscopy (ARPES) data on BaTiO₃ (BTO) films, we propose that the electric field of the ferroelectric bulk of the film induces WSL of the two-dimensional states present at the film surface. Furthermore, it will be shown that this effect can be extended to thin overlayers of SrTiO₃ (STO) where the ferroelectric field of the BTO substrate localizes the STO surface states.
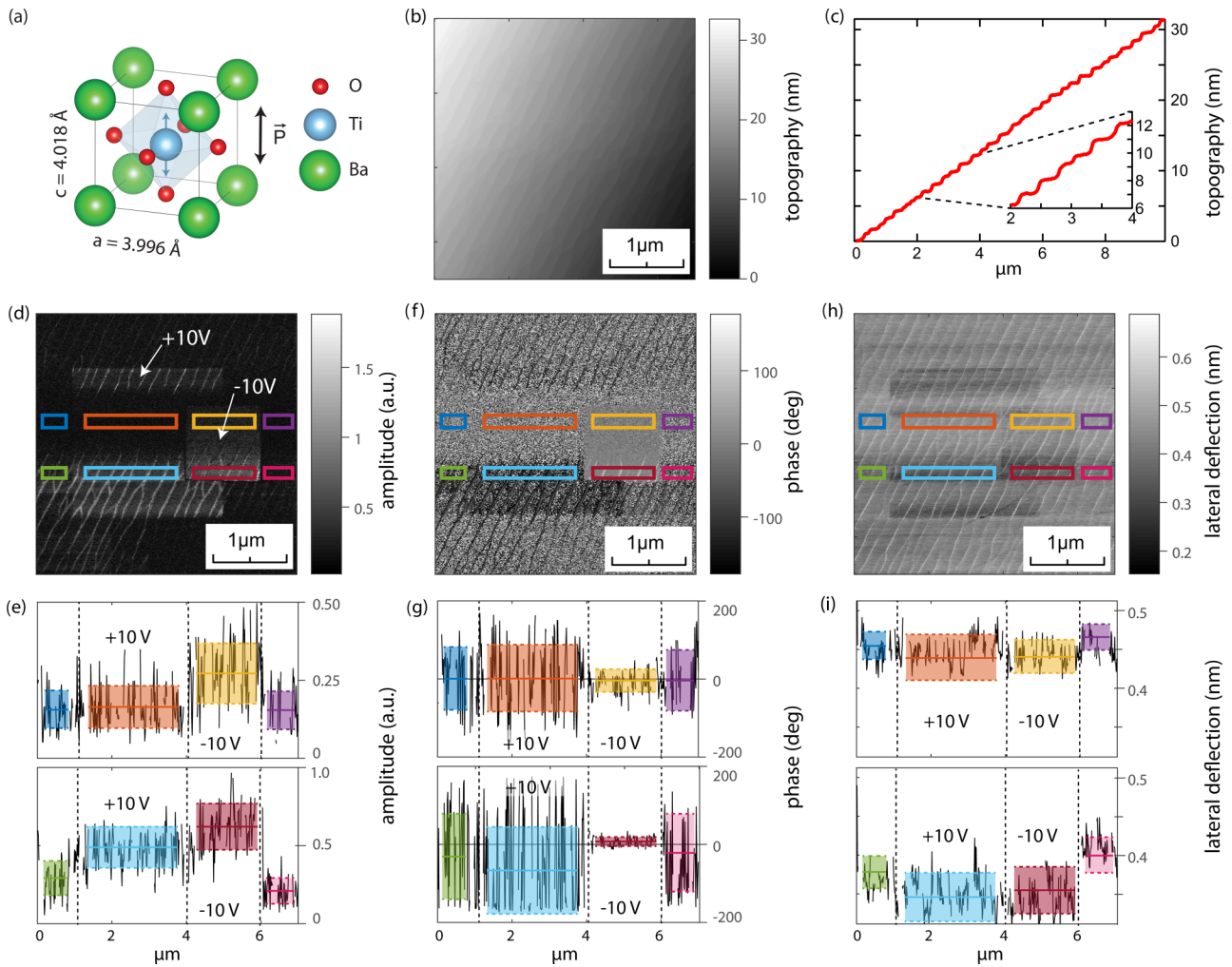
045132-1

FIG. 1. (a) Tetragonal BTO uc with indicated polarization axis. (b) PFM topography of 50 uc BTO grown on Nb:STO. (c) Topographic line profile along the diagonal perpendicular to the step edges. (d) PFM amplitude including written areas for $+10$ and -10 V applied to the tip, as indicated. (e) Line profiles along the center of the marked squares in (d) with average values and standard deviation of the marked areas indicated in Table I. (f) PFM phase with (g) line profiles and (h) lateral deflection with (i) line profiles.

BTO is a well-known ferroelectric material and closely related to the perovskites SrTiO$_3$, CaTiO$_3$ (CTO), and KTaO$_3$ (KTO). These materials are all known to host a two-dimensional electron gas at their surface [21–27]. Ferroelectric properties due to local lattice relaxations play, together with oxygen vacancies, a key role in the formation of the two-dimensional electron gas on the surfaces of these systems. These three perovskites are all classified as incipient ferro-electrics in which quantum fluctuations prevent a ferroelectric order [28–31]. Two-dimensional states can also be expected at the surface of BTO, which presents an excellent opportunity to study the impact of bulk ferroelectric order on these two-dimensional states at the surface and their transport properties [32]. It also offers a means of inducing ferroelectricity in other perovskites through doping or multilayer structure assembly. With the insights into fundamental transport mechanisms by the observation of WSL, new ways to directly manipulate and tailor transport properties of ferroelectric semiconductors become accessible.

Bulk crystalline BTO is ferroelectric below the transition temperature of 120 °C, exhibiting three different ferroelectric

phases [33,34]. Namely, the tetragonal phase [Fig. 1(a)] from 120 °C to 5 °C, the orthorhombic phase from 5 °C to −90 °C, and, for temperatures below −90 °C, the rhombohedral phase. Each of these phases has distinct electric-polarization anisotropies given by the symmetries of the unit cell (uc) [33,34]. The phase diagram of BTO thin films is significantly different compared to bulk BTO. In films, the transition temperature is raised for compressive as well as tensile strain [35]. For tensile strain, it has been demonstrated that solely an or-thorhombic phase exists below the ferroelectric transition tem-perature [35–37]. For compressive strain, the tetragonal phase [Fig. 1(a)] is the only ferroelectric phase present below the tran-sition temperature, with a preferred polarization along the out-of-plane axis in films with a thickness of around of 5 unit cells (uc) [37,38]. With increasing film thickness, strain and growth-defect relaxation will be responsible for a mixture of in-plane and out-of-plane domains of the tetragonal phase. In thicker films of BTO grown on STO, a mixture of domains with the size of around 20 nm can be observed as a result of relaxation [35,39]. Furthermore, the formation of domain walls with a 90° change in polarization direction are preferred energetically

TABLE I. Table with the average values and corresponding standard deviation for the line profile areas in Figs. 1(e), 1(g), and 1(i). The values correspond to going from left to right along the profile. The upper (lower) values correspond to the top (bottom) profile respectively.

	Unpoled	−10 V area	+10 V area	Unpoled
Amplitude	0.16 ± 0.06	0.16 ± 0.07	0.27 ± 0.10	0.15 ± 0.06
(arb. units)	0.29 ± 0.11	0.48 ± 0.13	0.62 ± 0.15	0.21 ± 0.08
Phase	2 ± 80	2 ± 86	-4 ± 29	-2 ± 78
(deg.)	-34 ± 109	-65 ± 111	7 ± 12	-25 ± 99
Lateral deflection	0.45 ± 0.02	0.44 ± 0.03	0.44 ± 0.02	0.47 ± 0.02
(nm)	0.38 ± 0.02	0.34 ± 0.03	0.35 ± 0.02	0.40 ± 0.02

to 180° domain walls [40]. This also favors a mixture of domains with out-of- and in-plane polarization directions.

II. METHODS

The films investigated in this work were grown by pulsed laser deposition (PLD), allowing a controlled layer-by-layer growth monitored by reflective high-energy electron diffraction (RHEED). Films with a thickness of 20 uc where grown on commercially available, single-terminated $SrTiO_3$, $Nb:SrTiO_3$, and $KTaO_3$ (001) substrates (SurfaceNet GmbH, see [41]). The growth was performed at a substrate temperature of 950 K, in a partial oxygen pressure of 1×10^{-5} mbar. STO films of 3- and 5-uc thickness were grown on top of this BTO film under similar conditions (see [41]). The samples were *in situ* transferred to the high-resolution ARPES end station and measured with circularly polarized synchrotron light. During the measurements the sample was held at 20 K and kept in ultrahigh-vacuum (UHV) conditions better than 1×10^{-10} mbar. The BTO films show a time-dependent behavior under UV irradiation. In order to turn the surface conductive and avoid charging, a path is written by the UV light starting from the mounting clamp to the center of the sample. This is an established experimental procedure for ARPES measurements of the two-dimensional (2D) states of titanates surfaces (see SOM of [25]).

The films were *ex situ* transferred to the NanoXAS beamline for piezoresponse force microscopy (PFM) measurements at room temperature under UHV conditions. The sample measured with PFM had a thickness of 50 uc and was grown on a 0.5 wt.% Nb-doped STO substrate under the same conditions as described above. A conductive substrate was chosen in order to have a well-defined back electrode and the higher film thickness in favor of a stronger PFM response signal.

III. FERROELECTRIC CHARACTERIZATION

The PFM topography in Fig. 1(b) shows a uniform sample surface with step heights [Fig. 1(c)] corresponding to one or multiple unit cells. The terrace width of 0.1–0.2 μm is given by the vicinality of the substrate, where a 0.2° miscut to the (001) surface was chosen to promote a layer-by-layer growth. The PFM phase and amplitude in Figs. 1(d) and 1(f) of the as-grown sample (bottom part of the field of view) shows no noticeable contrast, indicating that no intrinsic domains of resolvable size ($\gtrsim$20 nm) are present. After subsequent writing of the surface with +10 and −10 V applied to the probe tip, a phase and amplitude contrast is noticeable, proving

the presence of ferroelectric properties in our films. Due to the small PFM signal of the $BaTiO_3$ film, the measurements where performed at the resonance frequency of the PFM setup. This is causing a small crosstalk of the PFM phase and amplitude with the topography signal, responsible for the visibility of the step edges in the PFM channels. Furthermore, both of the written regions exhibit significant noise. In order to quantify the ferroelectric properties, two line profiles are taken along the scanning direction in the center of the marked, colored squares for the PFM amplitude [Fig. 1(e)] and phase [Fig. 1(g)] each. The signal in the vicinity of the step edges is excluded from the line profiles. In the amplitude line profiles a clear difference between the positively, the negatively, and the unwritten areas is noticeable. Especially the amplitude of the negative poled region is clearly higher than the positive and the unwritten areas. On the phase signal, a clear reduction of noise is noticeable for the negatively poled area, while for the positively poled part the noise is on the level of the unpoled region (see Table I). The phase difference between the oppositely poled area is 6° for the top row and 72° for the bottom row with an error margin larger than the difference. This difference is significantly less than the 180° phase difference expected for completely opposite polarized regions. The reason for this observation is a not completely homogeneously polarized surface in the written areas. This indicates a strong locking of the domains in the in-plane direction due to interface strain and relaxation mechanisms.

The PFM measurements show that writing with a negative potential applied to the probe tip has a more noticeable effect than writing with a positive potential. Especially the strong noise reduction for the phase and the offset in the amplitude is obvious. In the phase, the mean value of the negative written area is, as for the unwritten part, very close to 0°. This indicates that a larger portion of the intrinsic domains are polarized pointing out of the plane than into the plane. Thus, the writing with positive potential applied is less effective. In order to uniformly polarize the two areas by switching all the in-plane domains to the out-of-plane axis, a higher potential than 10 V would be needed. In the lateral deflection [Figs. 1(g) and 1(h)] of the probe tips a clear contrast is noticeable between the written regions and the unpoled area. This lowering of the friction at the previously written areas could be due to the reduction of in-plane domains in these regions changing the local polarization fields.

IV. PHOTOEMISSION RESULTS

The x-ray photoelectron spectroscopy (XPS) measured at normal emission and at a more surface-sensitive emission angle
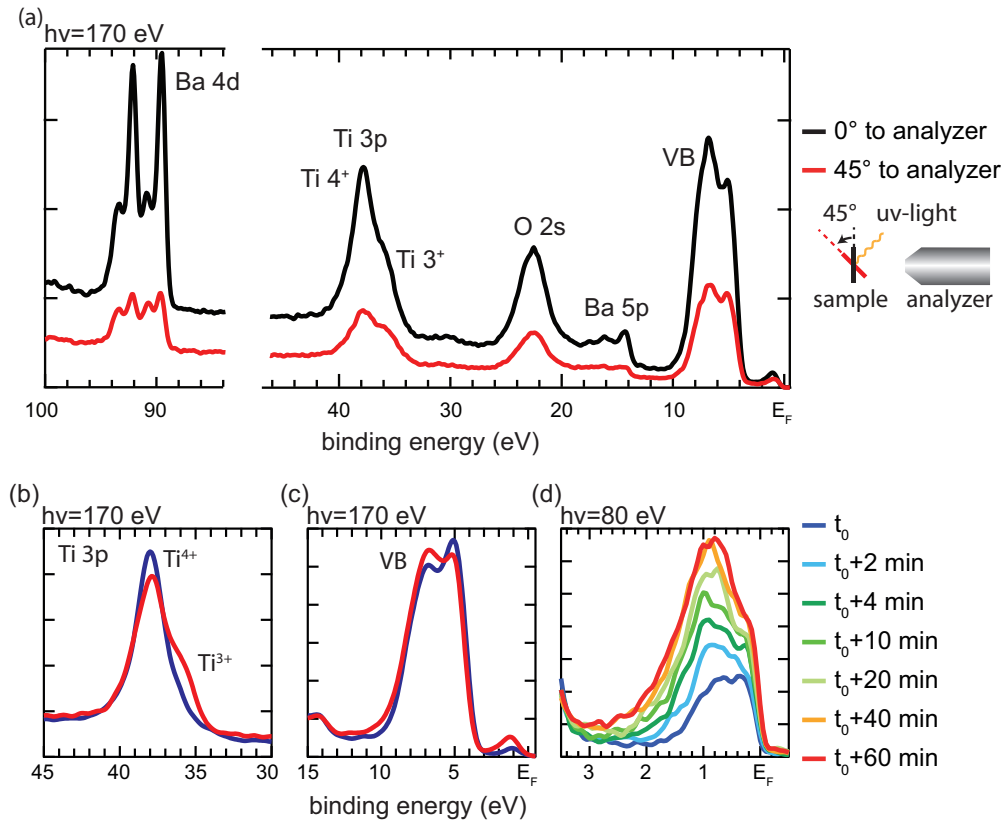
FIG. 2. (a) XPS measurements with $h\nu = 170$ eV photons for normal emission (black) and an emission angle of 45° (red). Time-dependent, angle-integrated photoemission intensity of the (b) Ti $3p$ core level (c) valence band, measured with $h\nu = 170$ eV and (d) in-gap and surface states, measured with $h\nu = 80$ eV.

of 45° show the Ba $4d$, Ti $3p$, and O $2s$ core levels [Fig. 2(a)]. The Ba $4d$ core level consists of the spin-orbit split Ba $4d_{3/2}$ and $4d_{5/2}$ doublet and a lower intensity doublet, shifted by 1.25 eV to higher binding energies. By comparing the peak areas of the two species for the two emission angles we can assign the higher binding energy, chemically shifted doublet to undercoordinated Ba ions in the BTO surface region [42–44]. The Ti $3p$ core level includes two peaks assigned to the Ti 4^+ and Ti 3^+ ions whereby the latter is more surface localized. Comparing the relative Ba $4d$ and Ti $3p$ peak areas for the two emission angles, we can conclude that the surface is TiO_2 terminated [45].

Close to the Fermi energy an in-gap state is located at a binding energy of 0.8 eV in the bulk band gap [46]. Under irradiation, the spectral intensity of this in-gap state and of the Ti 3^+ shoulder of the Ti $3p$ core level is increasing with time as shown in Figs. 2(b)–2(d). In case of the Ti 3^+, its percentage with respect to the total Ti $3p$ peak area rises from 7% to 18% within one hour [Fig. 2(b)]. This scales to a free charge carrier density at the surface of 0.18 electrons per uc after one hour, when saturation is reached. Within the same time frame, the intensity of the in-gap state increases by 300% [Figs. 2(c) and 2(d)]. The surface localized Ti 3^+ ions are linked to the creation of oxygen vacancies and structural reordering of the surface layers in the titanium-based perovskites [25]. The changes implied in the distortion of the TiO_6 octahedra and their respective binding angles due to the reordering will

alter the hybridization of titanium and oxygen. Indications of this change in hybridization are observable in the altering peak intensity of the valence band with time. The observed changes under UV light saturate within 30 min and are persistent with time regardless if the area is further irradiated or not.

Furthermore, a metallic state is visible as a second peak at the Fermi energy [Fig. 2(d)]. This only changes by 0.3% in peak area within the same time frame. Thus, although the intensity of Ti 3^+ and the in-gap state seems to be related, the intensity of the metallic states does not directly scale. The detailed properties of this metallic state will be the focus of the rest of this paper. It will be shown that this is a two-dimensional state at the surface of the BTO film and it is proposed that it becomes localized due to the strong in-plane ferroelectric fields in the bulk of the underlying film.

The ARPES measurements in Fig. 3 show metallic states emerging from the in-gap state. Resonant effects cause strong intensity modulations, but the states show no clear dispersion as a function of photon energy, indicating their two-dimensional nature [41,47–49]. As for STO, matrix element effects are responsible for the suppression of intensity at $k = 0$ due to the mainly xy symmetry of the two-dimensional state [41]. These states can be attributed to the partially filled Ti $3d_{xy}$ orbital, that is split from the Ti $3d_{xz}$ and Ti $3d_{yz}$ orbitals due to a distortion of the TiO_6 octahedron by lattice relaxation [21,25,27]. However, the Fermi surface around the $\overline{\Gamma}$ points
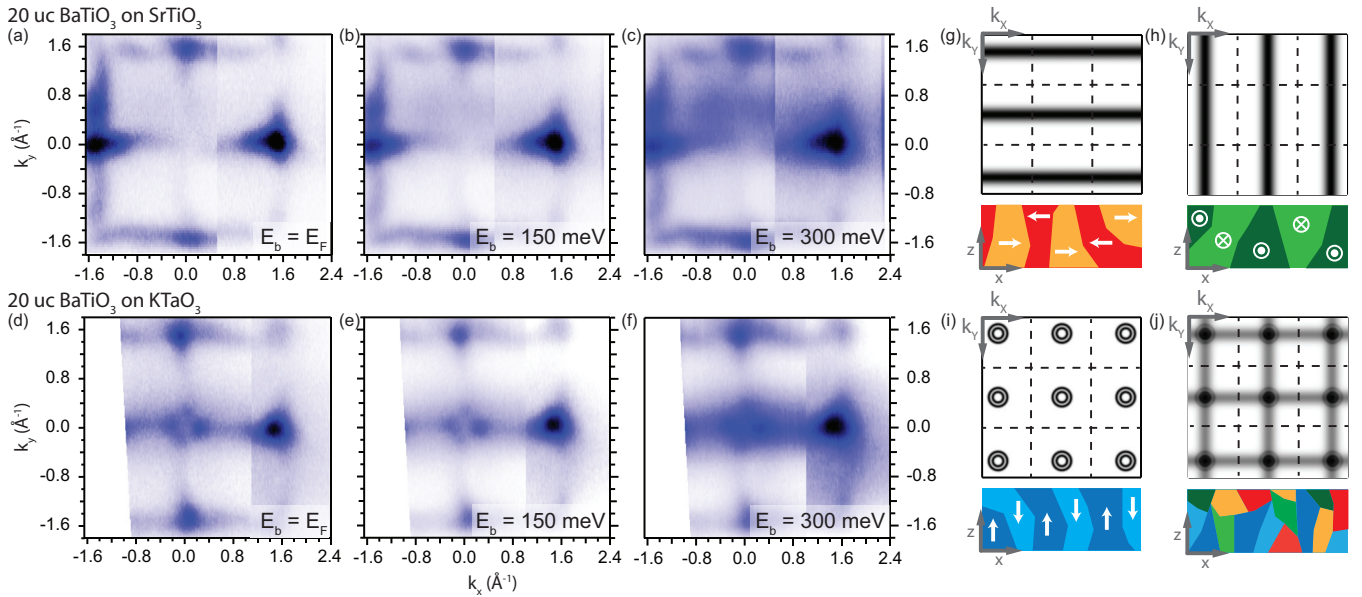
FIG. 3. (a)–(c) Constant energy surfaces of 20 uc of BTO grown on STO measured with $h\nu = 80$ eV for $E_b = E_F$ (a), $E_b = 150$ meV (b), and $E_b = 300$ meV (c). (d)–(f) Same as (a)–(c) for 20 uc BTO on KTO. (g)–(j) Different ferroelectric domain configurations of the films and the corresponding WSL states for in-plane polarizations along $\langle 100 \rangle$ (g) and $\langle 010 \rangle$ (h) and out-of-plane polarization along $\langle 001 \rangle$ (i). (j) Combined WSL states from the three configurations with equal weight.

shows no clear bands of the two-dimensional states but features spectral weight, elongated along both $\overline{\Gamma X}$ directions. These elongated states extend over multiple surface Brillouin zones connecting the neighboring Γ points as shown in Figs. 3(a) and 3(d). Comparing the Fermi surface with constant energy surfaces at higher binding energies [Figs. 3(b) and 3(c) and 3(e) and 3(f)], no dispersion of these states with respect to the binding energy is noticeable. As shown in Fig. 4(b) at 400 meV binding energy, the pattern observed at the Fermi energy is still visible, however, also spectral intensity around the $\overline{M}$ point, away from the Γ points and the $\overline{\Gamma X}$ direction, becomes apparent. At a binding energy of 800 meV, corresponding to the energy of the in-gap state of BTO as seen in Fig. 4(a) the checkerboard pattern observed at the Fermi energy is not distinguishable anymore. In Fig. 4(c) there is a constant intensity background with little structure except higher spectral intensities around the Γ points due to diffraction effects. This shows that the checkerboard pattern does not originate from the in-gap states.

In order to exclude that the observed pattern without a clear dispersion is a measurements artifact caused by the probing geometry, in Fig. 4(d) we present measurements where the crystal is aligned with $\overline{\Gamma M}$ parallel to the analyzer entrance slit. The angular scanning direction is perpendicular to the alignment direction and consequently different for the two cases. Apart from changes in the relative intensities, the altering of the measurement geometry does not affect the data. In particular, the localized states are still visible, smeared along the $\overline{\Gamma X}$ direction.

Quadratic-shaped constant energy surfaces have been observed in other TMOs with metallic bulk character [50,51]. In these cases the states directly follow the calculated band structure, possibly enhanced by the standing wave field and limited resolution, and are located at the Brillouin zone boundary and not the center. In contrast, any band structure calculation for BaTiO$_3$(001) predicts a circular or elliptical Fermi surface similar to what is observed for STO, CTO, and KTO [21–27], in strong contrast to our results.
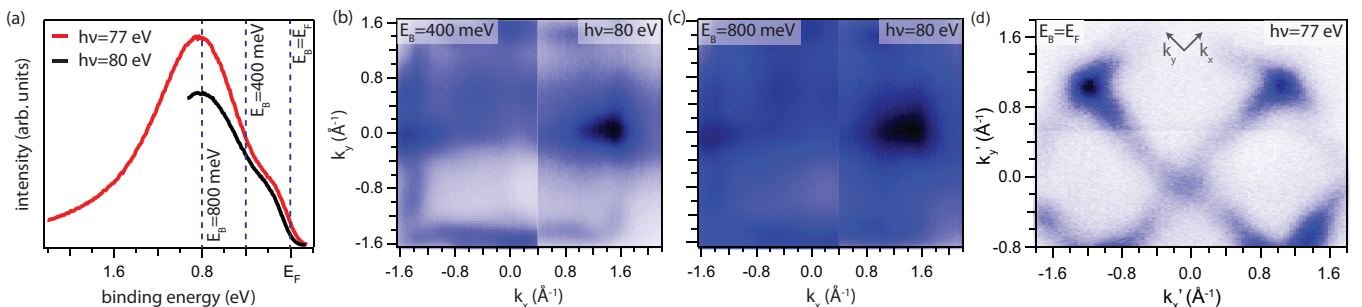

FIG. 4. (a) Energy distribution curves for $h\nu = 77$ eV and $h\nu = 80$ eV at $\overline{\Gamma_{10}}$. (b) Constant energy surface at a binding energy of $E_B = 400$ meV and (c) a binding energy of $E_B = 800$ meV which corresponds to the energy of the in-gap state. (d) Fermi surface of 10 uc BTO on STO for $h\nu = 77$ eV oriented with $\overline{\Gamma M}$ along the analyzer entrance slit.

In the related SrTiO₃(001) also d_{xz} and d_{yz} derived states are observed that are elongated along the $\overline{\Gamma X}$ direction, and the possibility that the nondispersive states around the Fermi level of BTO are of similar origin needs to be explored. A significant difference is that these states on STO clearly disperse with binding energy and show a parabolic shape [25], whereas on BTO no clear dispersion with binding energy can be discerned. More importantly, we can use the difference of selection rules for d_{xz}, d_{yz}, and d_{xy} derived states. Only states with mainly d_{xy} symmetry will show the observed node in intensity at $k_y = 0$ for p-polarized light and at $k_x = 0$ for s-polarized light throughout the Brillouin zone [41]. This is a strong indication that the states are of d_{xy} character and smeared along the x and y directions while still maintaining their orbital symmetry.

These observations and the comparison to related systems leads us to conclude that WSL is the most likely explanation for the measured checkerboard pattern. However, at this point we cannot exclude the possible influence of conductive domain walls [52–54] with well-defined perpendicular orientation, or other more exotic explanations.

V. WANNIER-STARK LOCALIZATION

As explained below, we suggest that the absence of in-plane dispersion of the states around the Fermi level is due to Wannier-Stark localization and a direct consequence of the electric field present in the bulk of the film. The electrons in the two-dimensional state experience an accelerating force in the direction opposite to the electric field present in the ferroelectric domains. Due to the potential barrier at unit-cell boundaries, the acceleration is not uniform but is described by Bloch oscillations [8,9]. This localizes the electron in real space and hence shows smearing in reciprocal space. Considering the lattice parameter of BTO, the condition $\tau > \tau_B$ for Bloch oscillations to exist is fulfilled for an electric field $F \gtrsim 10^9$ V/m assuming a typical relaxation time of $\tau = \lambda/v_F \approx 10^{-14}$ s [11], which exceeds the breakdown field strength of known insulators. Due to its ferroelectric properties, the local electric field at the BTO film surface is several order of magnitudes higher than any possible external electric field.

An estimate of the electric field inside BTO films can be obtained along the following lines. The external electric field of a ferroelectric material is given by its polarization P [11,55]. For bulk, tetragonal BTO the polarization is reported to be $P \approx 0.25$ C/m² [56] and is predicted to increase for strained films [57] which results in an external electric field of

$$|F| = \frac{P}{(\epsilon_r - 1)\epsilon_0} \approx 5 \times 10^8 \text{ V/m}. \tag{1}$$

The relative permittivity ϵ_r for thin films is reduced by several orders of magnitude compared to bulk BTO. For the resulting external electric field of Eq. (1), the reported value of $\epsilon_r \approx 60$ at 80 K for a 100-nm-thick film is taken as approximation for the relative permittivity of the films discussed in this work [58,59]. Based on the external electric field F, the local electric field F_{loc} inside the material is given as $F_{\text{loc}} = 1/3(\epsilon_r + 2)F$ [11]. With the relation (1) for the external electric field, the local

electric field can be written as a function of the polarization P:

$$|F_{\text{loc}}| = \frac{1}{3} \frac{P(\epsilon_r + 2)}{(\epsilon_r - 1)\epsilon_0} \approx \frac{1}{3} \frac{P}{\epsilon_0} \approx 1 \times 10^{10} \text{ V/m}. \tag{2}$$

The resulting local electric field in ferroelectric BTO is large enough for the occurrence of WSL. With a magnitude of $|F_{\text{loc}}| \approx 1 \times 10^{10}$ V/m the local electric field of BTO results in a Bloch oscillation time of $\tau_B = \frac{h}{eFa} \approx 1 \times 10^{-15}$ s within the unit cell of BTO ($a \approx 4$ Å). For a relaxation time of $\tau = 10^{-14}$ s, the condition $\tau > \tau_B$ is therefore satisfied in a unit cell of ferroelectric BTO and the occurrence of Bloch oscillations and Wannier-Stark localization is expected. It should be noted that due to the localization of the electrons, no net charge transport is expected.

In this discussion we started from a more macroscopic real-space transport model and considered the microscopic consequences and how this looks in reciprocal space. However, one can also start from a band structure model and reach the same picture. In this case, the Bloch oscillation can be regarded as a momentum-independent Bragg reflection, which normally only occurs at the Brillouin zone boundary. Thus, the group velocity becomes zero for all momenta and the bands are flattened out.

In general, the WSL is accompanied by the formation of a Wannier-Stark ladder, a set of electron states separated in energy and space. In superlattices, where a WSL occurs by the help of an externally applied, tunable electric field, indications of a Wannier-Stark ladder are observed [13,14]. The energy separation between the steps of the Wannier-Stark ladder is given as $\Delta E = eFa$ [10,11] and expected to be between 0.1–6 eV for the films studied, based on an electric field between 5×10^8 V/m to 1.5×10^{10} V/m. With the origin of the electric field in the ferroelectric properties of BTO, the local electric field is not expected to be constant due to the variable domain configurations and sizes. Therefore, the energy steps of the resulting Wannier-Stark ladder are not isotropic but will vary within the probed area. Therefore, ARPES is not the method of choice to observe these ladders due to the limited coherence length of these states. Local probe techniques using tunneling or optical spectroscopy should be able to address this aspect in future work.

On the other hand, due to the surface localization of the Bloch oscillations in the BTO films, the observation of the WS ladder is beyond the compatibility of conventional techniques [12–17]. For such surface or interface systems the WSL-induced smearing observed by ARPES can provide an alternative method to observe these effects.

The BTO films grown on a STO substrate have a compressive strain of 2% at the interface. As a result, the film is expected to stay in a single tetragonal phase below the ferroelectric phase transition [37,38]. Tetragonal BTO can host a ferroelectric polarization along the ⟨001⟩ out-of-plane as well as the ⟨100⟩ and ⟨010⟩ in-plane directions. While at the interface the polarization direction is preferably along the out-of-plane axis, strain relaxation mediated by growth defects will be responsible for a mixture of domains close to the film surface. The domains with different electric field directions will all contribute differently to the Fermi surface. The in-plane domains, exhibiting an electric field along ⟨100⟩ [Fig. 3(g)]
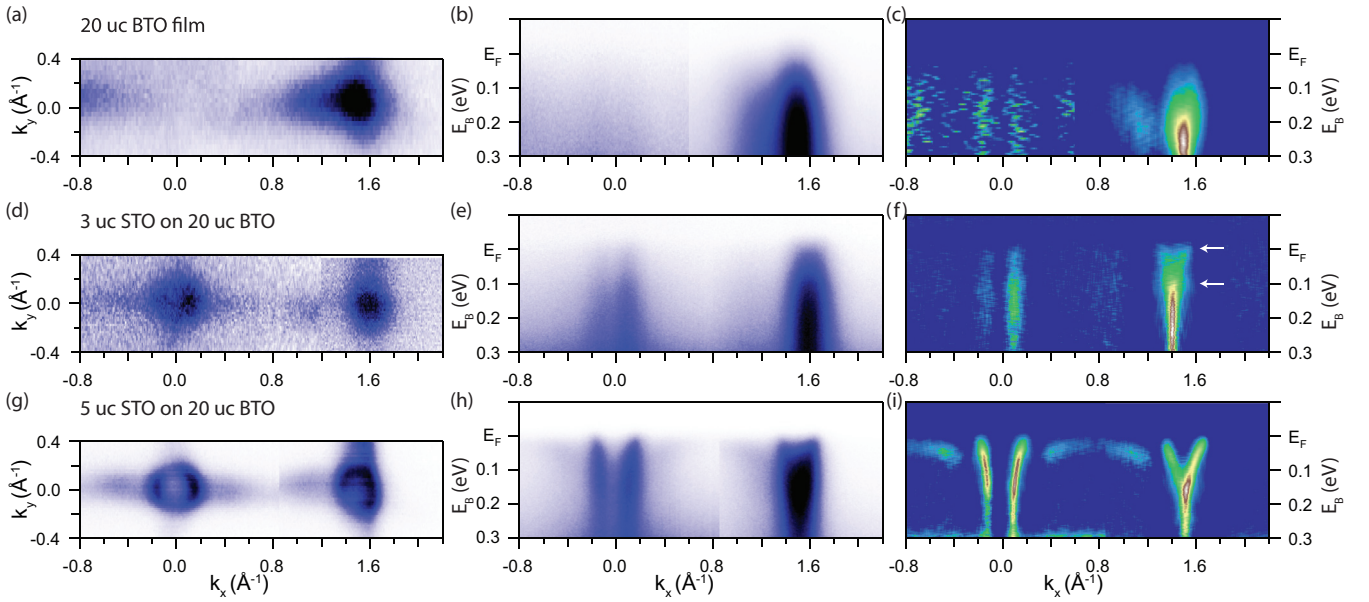
FIG. 5. (a), (d), (g) Fermi surface, (b), (e), (h) band map at $k_y = 0$ Å^{-1}, and (c), (f), (i) two-dimensional curvature [60] measured at $h\nu = 82$ eV. (a)–(c) For the 20-uc BTO film, (d)–(f) for a 3-uc STO film on top of 20 uc of BTO, and (g)–(i) for a 5-uc STO film on top of 20 uc of BTO. The arrows in (f) indicate the polaron replica.

or $\langle 010 \rangle$ [Fig. 3(h)] directions will both give rise to WSL. In ARPES, this WSL becomes visible as one-dimensional states along the $\overline{\Gamma X}$ directions. In domains where the electric field is along the out-of-plane or $\langle 001 \rangle$ directions [Fig. 3(i)], the electric field will lift the spin degeneracy of the two-dimensional states. The resulting Rashba-type spin splitting consists of oppositely spin-polarized, concentric rings at the Fermi surface [5,61,62]. The direction of the spin polarization of the bands will be inverted depending on the sign of the ferroelectric polarization vector.

With a domain size on the order of 20 nm [39], the synchrotron beam with a size of around 100 μm will average over many domains with different ferroelectric polarization directions. The resulting model Fermi surface in Fig. 3(j), formed by an overlay of the contributions from the different domains, is in good agreement with the ARPES measurements. The combination of dipole selection rules and the smearing due to WSL changes the observed lines from single to double depending on the light polarization [41].

For BTO films grown on KTO, the compressive strain is reduced to 0.2% due to the larger lattice constant of KTO compared to STO. With the change in strain also the domain formation is expected to be different for the BTO films on KTO. Furthermore, our KTO substrates have a higher step density as our STO substrates inducing an imbalance between different domains [41]. When comparing the data of the BTO film on KTO [Figs. 3(d)–3(f)] with the results of the film grown on STO [Figs. 3(a)–3(c)] the clearest difference is the signature of a circular Fermi surface contribution around $\overline{\Gamma_{00}}$. This observation is in agreement with an altered domain configuration. The reduced interface strain and the higher step density are responsible for the formation of larger domains with a higher fraction polarized along the z directions in the measured BTO films grown on KTO.

This dependency on the domain structure makes ARPES a promising alternative to study ferroelectric domains that are not easily accessible by other techniques. For example, a similar checkerboard pattern was observed in ARPES, but not interpreted as WSL, on GdTiO$_3$/SrTiO$_3$ superlattices [63]. No circular Fermi surface around the $\overline{\Gamma}$ points is observed, in line with predicted purely in-plane ferroelectric domains for this system [64].

VI. STO OVERLAYERS

The general nature of the proposed WSL is further illustrated by its presence in ultrathin STO films grown on top of the BTO layers. In Fig. 6 a comparison of XPS spectra is shown for the clean BTO films and 3 and 5 uc of STO grown on top. The data were normalized to the background after the O 2s core level and the BTO data were offset in Fig. 6(a) for clarity. As expected, the Sr core levels increase with STO coverage whereas the Ba core levels show an exponential decay with coverage and are almost completely suppressed for the 5-uc-thick STO film. This indicates a layer-by-layer growth of a closed STO film on top of the BTO substrate. The small changes of binding energies in the Ba 4d core levels could give insight in the detailed atomic structure of the BTO/STO interface and possible intermixing in the first unit cell. However, this goes far beyond the scope of this work and is best combined with detailed structural investigations.

The ARPES data for a 3-uc-thick STO film in Figs. 5(d)–5(f) exhibits states very similar to pure BTO Figs. 5(a)–5(c). The Fermi surface shows stripes extending over several surface Brillouin zones (see [41]) characteristic for WSL. However, the reduced electric field with increasing STO film thickness
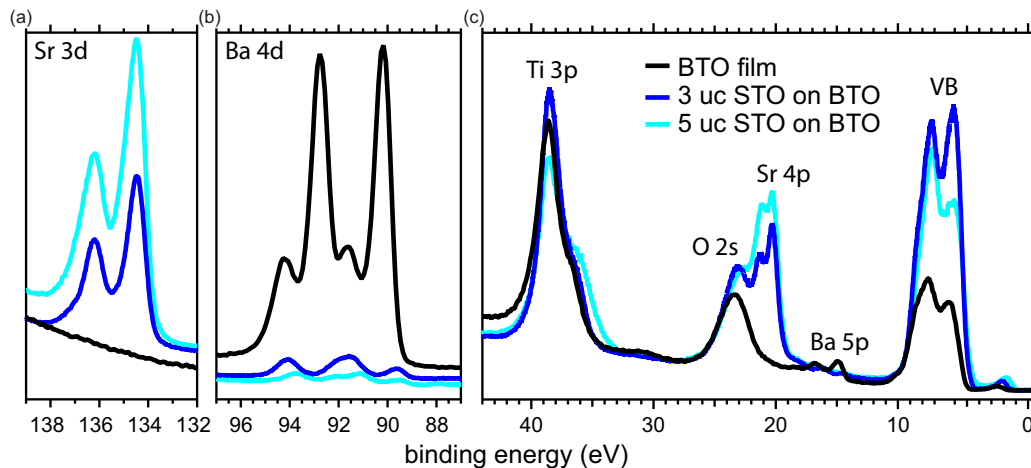
FIG. 6. XPS spectra obtained with $h\nu = 170$ eV for the clean BTO film and with 3 and 5 uc of STO on top. (a) Sr $3d$, (b) Ba $4d$, (c) Ti $3p$, O $2s$, Sr $4p$, Ba $5p$, and the valence band.

results in a lower intensity of the smearing and a shallow electron pocket with polaron replicas [65,66] becomes visible [see markers in Fig. 5(f)]. For the surface of the 5-uc film in Figs. 5(g)–5(i) the fields of the BTO substrate are so far reduced that no indication of WSL is visible. The ARPES data resemble the electronic structure of bulk STO with the more filled circular d_{xy} states forming the two-dimensional electron gas (2DEG) and elongated d_{xz} and d_{yz} states that clearly disperse with binding energy [Figs. 5(h) and 5(i)] [25]. The only difference is that the d_{xz} and d_{yz} states appear at a higher binding energy of 100 meV instead of 50 meV, indicating a possible structural difference between the two systems.

From these results we can conclude that either up to 3 uc of STO on BTO are ferroelectric, or that about 4 uc of STO are needed to let the electric field of BTO decay to a value that no longer influences the electronic properties at the sample surface. Furthermore, the sharp electronlike states at the surface of the STO films verify the high-crystalline quality also of our BTO layer. RHEED (see [41]) and XPS data (Fig. 6) both indicate a layer-by-layer growth of the STO, opening the possibility to study whether a ferroelectric order is induced in the STO by high-resolution transmission electron microscopy in future work.

VII. CONCLUSIONS

To conclude, we have presented combined effects of two different physical properties on BTO film surfaces: the formation of a two-dimensional state and the interpretation of the measured Fermi surface as Wannier-Stark localization of this state. We have further demonstrated that ARPES can provide a novel means of probing WSL in reciprocal space. The combined presence of electric fields and two-dimensional states at the surface of a transition metal oxide opens up a rich field to study the interplay of ferroelectricity and interface states. For the study of the macroscopic influence of WSL on the transport properties, BTO films with preferred polarization directions should be prepared by the help of different substrates regarding orientation, lattice parameters, and conductivity [67–69] and under different growth conditions [46]. Furthermore, our experiments suggest that WSL could be a general effect for ferroelectric materials with surface or interface states, and domains with an in-plane electric field.

[1] T. Kolodiazhnyi, M. Tachibana, H. Kawaji, J. Hwang, and E. Takayama-Muromachi, Phys. Rev. Lett. **104**, 147602 (2010).

[2] J. Hwang, T. Kolodiazhnyi, J. Yang, and M. Couillard, Phys. Rev. B **82**, 214109 (2010).

[3] Y. Wang, X. Liu, J. D. Burton, S. S. Jaswal, and E. Y. Tsymbal, Phys. Rev. Lett. **109**, 247601 (2012).

[4] D. Di Sante, P. Barone, R. Bertacco, and S. Picozzi, Adv. Mater. **25**, 509 (2013).

[5] J. Krempaský, H. Volfová, S. Muff, N. Pilet, G. Landolt, M. Radović, M. Shi, D. Kriegner, V. Holý, J. Braun, H. Ebert, F. Bisti, V. A. Rogalev, V. N. Strocov, G. Springholz, J. Minár, and J. H. Dil, Phys. Rev. B **94**, 205111 (2016).

[6] J. Krempaský, S. Muff, J. Minár, N. Pilet, M. Fanciulli, A. P. Weber, E. B. Guedes, M. Caputo, E. Müller, V. V. Volobuev, M. Gmitra, C. A. F. Vaz, V. Scagnoli, G. Springholz, and J. H. Dil, Phys. Rev. X **8**, 021067 (2018).

[7] C. Cheng, J.-T. Sun, X.-R. Chen, H.-X. Fu, and S. Meng, Nanoscale **8**, 17854 (2016).

[8] F. Bloch, Z. Phys. **52**, 555 (1929).

[9] C. Zener, Proc. R. Soc. A **145**, 523 (1934).

[10] M. P. Marder, *Condensed Matter Physics*, 2nd ed. (Wiley, Hoboken, NJ, 2010).

[11] P. Hofmann, *Solid State Physics: An Introduction* (Wiley-VCH, Weinheim, 2014).

[12] L. Esaki and R. Tsu, IBM J. Res. Dev. **14**, 61 (1970).

[13] E. E. Mendez, F. Agulló-Rueda, and J. M. Hong, Phys. Rev. Lett. **60**, 2426 (1988).

[14] P. Voisin, J. Bleuse, C. Bouche, S. Gaillard, C. Alibert, and A. Regreny, Phys. Rev. Lett. **61**, 1639 (1988).

[15] G. von Plessen and P. Thomas, Phys. Rev. B **45**, 9185 (1992).

[16] J. Feldmann, K. Leo, J. Shah, D. A. B. Miller, J. E. Cunningham, T. Meier, G. von Plessen, A. Schulze, P. Thomas, and S. Schmitt-Rink, Phys. Rev. B **46**, 7252 (1992).

[17] C. Waschke, H. G. Roskos, R. Schwedler, K. Leo, H. Kurz, and K. Köhler, Phys. Rev. Lett. **70**, 3319 (1993).

[18] M. Ben Dahan, E. Peik, J. Reichel, Y. Castin, and C. Salomon, Phys. Rev. Lett. **76**, 4508 (1996).

[19] Z. A. Geiger, K. M. Fujiwara, K. Singh, R. Senaratne, S. V. Rajagopal, M. Lipatov, T. Shimasaki, R. Driben, V. V. Konotop, T. Meier, and D. M. Weld, Phys. Rev. Lett. **120**, 213201 (2018).

[20] O. Schubert, M. Hohenleutner, F. Langer, B. Urbanek, C. Lange, U. Huttner, D. Golde, T. Meier, M. Kira, S. W. Koch *et al.*, Nat. Photonics **8**, 119 (2014).

[21] A. F. Santander-Syro, O. Copie, T. Kondo, F. Fortuna, S. Pailhès, R. Weht, X. G. Qiu, F. Bertran, A. Nicolaou, A. Taleb-Ibrahimi, P. L. Fèvre, G. Herranz, M. Bibes, N. Reyren, Y. Apertet, P. Lecoeur, A. Barthélémy, and M. J. Rozenberg, Nature (London) **469**, 189 (2011).

[22] W. Meevasana, P. D. C. King, R. H. He, S.-K. Mo, M. Hashimoto, A. Tamai, P. Songsirititthigul, F. Baumberger, and Z.-X. Shen, Nat. Mater. **10**, 114 (2011).

[23] P. D. C. King, R. H. He, T. Eknapakul, P. Buaphet, S. K. Mo, Y. Kaneko, S. Harashima, Y. Hikita, M. S. Bahramy, C. Bell, Z. Hussain, Y. Tokura, Z. X. Shen, H. Y. Hwang, F. Baumberger, and W. Meevasana, Phys. Rev. Lett. **108**, 117602 (2012).

[24] A. F. Santander-Syro, C. Bareille, F. Fortuna, O. Copie, M. Gabay, F. Bertran, A. Taleb-Ibrahimi, P. Le Fèvre, G. Herranz, N. Reyren, M. Bibes, A. Barthélémy, P. Lecoeur, J. Guevara, and M. J. Rozenberg, Phys. Rev. B **86**, 121107 (2012).

[25] N. C. Plumb, M. Salluzzo, E. Razzoli, M. Månsson, M. Falub, J. Krempasky, C. E. Matt, J. Chang, M. Schulte, J. Braun, H. Ebert, J. Minár, B. Delley, K.-J. Zhou, T. Schmitt, M. Shi, J. Mesot, L. Patthey, and M. Radović, Phys. Rev. Lett. **113**, 086801 (2014).

[26] T. C. Rödel, F. Fortuna, S. Sengupta, E. Frantzeskakis, P. L. Fèvre, F. Bertran, B. Mercey, S. Matzen, G. Agnus, T. Maroutian, P. Lecoeur, and A. F. Santander-Syro, Adv. Mater. **28**, 1976 (2016).

[27] S. Muff, M. Fanciulli, A. P. Weber, N. Pilet, Z. Ristić, Z. Wang, N. C. Plumb, M. Radović, and J. H. Dil, Appl. Surf. Sci. **432**, 41 (2018).

[28] H. Weaver, J. Phys. Chem. Solids **11**, 274 (1959).

[29] K. A. Müller and H. Burkard, Phys. Rev. B **19**, 3593 (1979).

[30] W. Zhong and D. Vanderbilt, Phys. Rev. B **53**, 5047 (1996).

[31] V. Lemanov, A. Sotnikov, E. Smirnova, M. Weihnacht, and R. Kunze, Solid State Commun. **110**, 611 (1999).

[32] Y. Urakami, M. Yamato, and Y. Watanabe, Ferroelectrics **346**, 32 (2007).

[33] W. J. Merz, Phys. Rev. **76**, 1221 (1949).

[34] P. R. Potnis, N.-T. Tsou, and J. E. Huber, Materials **4**, 417 (2011).

[35] Y. Li and L. Chen, Appl. Phys. Lett. **88**, 072905 (2006).

[36] D. A. Tenne, X. X. Xi, Y. L. Li, L. Q. Chen, A. Soukiassian, M. H. Zhu, A. R. James, J. Lettieri, D. G. Schlom, W. Tian, and X. Q. Pan, Phys. Rev. B **69**, 174101 (2004).

[37] J. Dionot, G. Geneste, C. Mathieu, and N. Barrett, Phys. Rev. B **90**, 014107 (2014).

[38] J. Paul, T. Nishimatsu, Y. Kawazoe, and U. V. Waghmare, Phys. Rev. Lett. **99**, 077601 (2007).

[39] C. Dubourdieu, J. Bruley, T. M. Arruda, A. Posadas, J. Jordan-Sweet, M. M. Frank, E. Cartier, D. J. Frank, S. V. Kalinin, A. A. Demkov *et al.*, Nat. Nanotechnol. **8**, 748 (2013).

[40] J. Dionot, Topology of ferroelectric polarization at the BaTiO$_3$(001) surface from ab initio calculations and electron microscopy-spectroscopy, Ph.D. thesis, Universite Paris Sud-Paris XI, 2015.

[41] See Supplemental Material at http://link.aps.org/supplemental/10.1103/PhysRevB.98.045132 for more detailed PFM analysis, estimation of the electric field, additional ARPES data of the BTO films, and further characterization data of the STO thin films.

[42] K. Jacobi, C. Astaldi, B. Frick, and P. Geng, Phys. Rev. B **36**, 3079 (1987).

[43] L. T. Hudson, R. L. Kurtz, S. W. Robey, D. Temple, and R. L. Stockbauer, Phys. Rev. B **47**, 10832 (1993).

[44] M.-Q. Cai, J.-C. Liu, G.-W. Yang, X. Tan, Y.-L. Cao, W.-Y. Hu, L.-L. Wang, and Y.-G. Wang, Surf. Sci. **601**, 1345 (2007).

[45] M. Radovic, N. Lampis, F. Miletto Granozio, P. Perna, Z. Ristic, M. Salluzzo, C. Schlepütz, and U. Scotti di Uccio, Appl. Phys. Lett. **94**, 022901 (2009).

[46] J. E. Rault, J. Dionot, C. Mathieu, V. Feyer, C. M. Schneider, G. Geneste, and N. Barrett, Phys. Rev. Lett. **111**, 127602 (2013).

[47] K. E. Smith and V. E. Henrich, Phys. Rev. B **38**, 9571 (1988).

[48] J. Tao, T. Luttrell, and M. Batzill, Nat. Chem. **3**, 296 (2011).

[49] U. Fano, Phys. Rev. **124**, 1866 (1961).

[50] A. X. Gray, J. Minár, L. Plucinski, M. Huijben, A. Bostwick, E. Rotenberg, S. Yang, J. Braun, A. Winkelmann, G. Conti *et al.*, Europhys. Lett. **104**, 17004 (2013).

[51] D. Eiteneer, G. K. Pálsson, S. Nemšák, A. X. Gray, A. M. Kaiser, J. Son, J. LeBeau, G. Conti, A. A. Greer, A. Keqi *et al.*, J. Electron Spectrosc. Relat. Phenom. **211**, 70 (2016).

[52] D. Meier, J. Seidel, A. Cano, K. Delaney, Y. Kumagai, M. Mostovoy, N. A. Spaldin, R. Ramesh, and M. Fiebig, Nat. Mater. **11**, 284 (2012).

[53] T. Sluka, A. K. Tagantsev, P. Bednyakov, and N. Setter, Nat. Commun. **4**, 1808 (2013).

[54] J. A. Mundy, J. Schaab, Y. Kumagai, A. Cano, M. Stengel, I. P. Krug, D. M. Gottlob, H. Doğanay, M. E. Holtz, R. Held, Z. Yan, E. Bourret, C. M. Schneider, D. G. Schlom, D. A. Muller, R. Ramesh, N. A. Spaldin, and D. Meier, Nat. Mater. **16**, 622 (2017).

[55] R. Feynman, R. Leighton, and M. Sands, *Feynman Lectures on Physics* (Addison-Wesley, Boston, 1964), Vol. 2.

[56] W. J. Merz, Phys. Rev. **91**, 513 (1953).

[57] C. Ederer and N. A. Spaldin, Phys. Rev. Lett. **95**, 257601 (2005).

[58] T. Hayashi, N. Oji, and H. Maiwa, Jpn. J. Appl. Phys. **33**, 5277 (1994.

[59] O. Trithaveesak, J. Schubert, and C. Buchal, J. Appl. Phys. **98**, 114101 (2005).

[60] P. Zhang, P. Richard, T. Qian, Y.-M. Xu, X. Dai, and H. Ding, Rev. Sci. Instrum. **82**, 043712 (2011).

[61] J. H. Dil, J. Phys.: Condens. Matter **21**, 403001 (2009).

[62] A. Santander-Syro, F. Fortuna, C. Bareille, T. Rödel, G. Landolt, N. Plumb, J. Dil, and M. Radović, Nat. Mater. **13**, 1085 (2014).

[63] S. Nemšák, G. Conti, A. X. Gray, G. K. Palsson, C. Conlon, D. Eiteneer, A. Keqi, A. Rattanachata, A. Y. Saw *et al.*, Phys. Rev. B **93**, 245103 (2016).

[64] S. Y. Park and A. J. Millis, arXiv:1505.04183.

[65] S. Moser, L. Moreschini, J. Jaćimović, O. S. Barišić, H. Berger, A. Magrez, Y. J. Chang, K. S. Kim, A. Bostwick, E. Rotenberg, L. Forró, and M. Grioni, Phys. Rev. Lett. **110**, 196403 (2013).

[66] Z. Wang, S. M. Walker, A. Tamai, Y. Wang, Z. Ristic, F. Y. Bruno, A. De La Torre, S. Riccò, N. Plumb, M. Shi *et al.*, Nat. Mater. **15**, 835 (2016).

[67] J. Sinsheimer, S. Callori, B. Ziegler, B. Bein, P. Chinta, A. Ashrafi, R. Headrick, and M. Dawber, Appl. Phys. Lett. **103**, 242904 (2013).

[68] J. Chen, Y. Luo, X. Ou, G. Yuan, Y. Wang, Y. Yang, J. Yin, and Z. Liu, J. Appl. Phys. **113**, 204105 (2013).

[69] R. Guo, L. Shen, H. Wang, Z. Lim, W. Lu, P. Yang, Ariando, A. Gruverman, T. Venkatesan, Y. P. Feng, and J. Chen, Adv. Mater. Interfaces **3**, 1600737 (2016).